

A Journal of the Gesellschaft Deutscher Chemiker

Angewandte Chemie

GDCh

International Edition

www.angewandte.org

Accepted Article

Title: Metal-Free PAZE-NH₄X₃·H₂O Perovskite for Flexible Transparent X-ray Detection and Imaging

Authors: Zhizai Li, Guoqiang Peng, Huanyu Chen, Chang Shi, Zhenhua Li, and Zhiwen Jin

This manuscript has been accepted after peer review and appears as an Accepted Article online prior to editing, proofing, and formal publication of the final Version of Record (VoR). The VoR will be published online in Early View as soon as possible and may be different to this Accepted Article as a result of editing. Readers should obtain the VoR from the journal website shown below when it is published to ensure accuracy of information. The authors are responsible for the content of this Accepted Article.

To be cited as: *Angew. Chem. Int. Ed.* **2022**, e202207198

Link to VoR: <https://doi.org/10.1002/anie.202207198>

Metal-Free PAZE-NH₄X₃·H₂O Perovskite for Flexible Transparent X-ray Detection and Imaging

Zhizai Li¹, Guoqiang Peng¹, Huanyu Chen¹, Chang Shi¹, ZhenHua Li², Zhiwen Jin^{1,*}

Dr. Z. Li, Dr. G. Peng, Dr. H. Chen, Dr. C. Shi, Prof. Z. Jin

¹School of Physical Science and Technology & College of Chemistry and Chemical Engineering & Key Laboratory for Magnetism and Magnetic Materials of the Ministry of Education, Lanzhou University, Lanzhou 730000, China

Prof. Z. H. Li

²School of Physical Science and Technology & Lanzhou Center for Theoretical Physics & Key Laboratory of Theoretical Physics of Gansu Province, Lanzhou University, Lanzhou 730000, China

E-mail: jinzw@lzu.edu.cn

Keywords: Flexible, Imaging, Metal-free, Perovskite, X-ray detection

Abstract

Metal-free perovskites have arisen great interest for their chemical diversity and eco-friendly properties, and recently expanded into X-ray detection for superior carrier behavior. However, the size and shape complexity of organic components results in the difficulties on evaluating their stability from theoretical considerations in high-energy radiation. Herein, we introduce multiple hydrogen-bonds metal-free PAZE-NH₄X₃·H₂O perovskite, where H₂O leads to more hydrogen bonds appearing between organic molecules and perovskite host. Suggested by the theoretical calculations, multiple hydrogen bonds promote the stiffness of lattice, and increase the diffusion barrier to inhibit ionic migration. Then, low trap density, high $\mu\tau$ products and structural flexibility of PAZE-NH₄Br₃·H₂O impel us to expand it into the flexible X-ray detector with the highest sensitivity of 3708 $\mu\text{C Gy}_{\text{air}}^{-1} \text{cm}^{-2}$, ultra-low detection limit of 0.19 $\mu\text{Gy}_{\text{air}}^{-1} \text{s}^{-1}$ and superior spatial resolution of 5.0 lp mm⁻¹.

Introduction

Sensitive X-ray detectors with high performance, durability and long-term stability, have enriched and guaranteed our daily lives in homeland security, nondestructive inspection, and medical diagnostics aspects.^[1-3] As one of the excellent candidate materials, metal halides perovskites (MHP) exhibit extraordinary detection properties owing to their high X-ray stopping power, superior defect tolerance and large mobility-lifetime ($\mu\tau$) product.^[4-6] Moreover, the low-temperature solution process further makes them compatible with the readout system of application-specific integrated circuits (ASICs).^[7] Although tremendous breakthrough has been made in high-performance MHP-based X-ray detection with advanced sensitivity reaching $2.1 \times 10^4 \mu\text{C Gy}_{\text{air}}^{-1} \text{cm}^{-2}$, the inevitable toxicity comes from solvents, including N, N-dimethylformamide (DMF), gamma-butyrolactone (γ -GBL) and chlorobenzene, and toxic metal ions (Pb^{2+} , Cd^{2+} , etc) would limit their application in wearable device and environment-friendly products.^[8-10] Besides, the uncontrollable ionic migration in the MHP-based X-ray detection further limits their key parameters, especially in the lowest detection limit and sensitivity.^[11]

A promising way to conquer these problems is to develop the non-toxic metal-free halide organic perovskite with an ABX_3 (or ABX_3C) perovskite structure, which recently emerged as a novel member of the perovskite family for X-ray detection, and can be obtained and degraded by non-toxic aqueous solution under room-temperature (RT). Moreover, beneficial to their unique perovskite structures, it not only possesses the basic advantages of perovskite materials but also shows chemical diversity,

tunability and lightweight of organic materials.^[12,13] These unique properties further make them present great prospects for bio-compatible, lightweight and eco-friendly preparation and application.^[14,15] Recently, their potential application for X-ray detection was also explored for their superior photoelectric properties in terms of long carrier diffusion length of several tens of microns, which were comparable to or better than the MHP-based materials.^[12] Besides, the high bulk resistivity (10^8 – 10^9 Ω cm), large bandgap (> 4 eV) and excellent X-ray stopping ability further broaden their application in X-ray field.^[15]

The first metal-free perovskites of PAZE-NH₄Cl₃·H₂O (PAZE = piperazinium, C₄N₂H₁₂) and DABCO-NH₄Cl₃ (DABCO = N-N'-diazabicyclo[2.2.2]octonium, C₆N₂H₁₄) were discovered by Bremner et al. in 2002, and simply investigated their crystal configuration and structural analysis for predicting its possible ferroelectric behavior.^[16] Later, Li et al. simply researched the electronic structures of PAZE-NH₄X₃·H₂O (X= Cl, Br, I) and highlight their superiority in elastic properties by theoretical calculation.^[17] However, the studies on their functions and applications are blank for almost two decades. Until 2018, Ye et al. novelly introduced a series of metal-free perovskites ferroelectrics and first time revealed their application by elaborating their polarization properties and phase-transition temperature.^[18] Subsequently, their photoelectric, ferroelectric and mechanical properties were systematically explored as well.^[19-21] Recently, Cui et al. firstly expanded them into X-ray detection, and studied the function of hydrogen bonds in the metal-free perovskites of DABCO-NH₄X₃ (DABCO = N-N'-diazabicyclo[2.2.2]octonium) with different halide anions.^[12] It is

found that hydrogen bonding influenced the charge transport mobilities, and the structural stiffness of metal-free perovskites because of the changed crystal packing behaviors, which drove molecular self-assembly to co-crystals.^[17] However, the crystal structures of metal-free perovskite are different from the MHP, where the components of the latter are mainly held together by hydrogen bonding, which plays a significant role in establishing the whole framework.^[16,18] Subsequently, they found that adding methyl group into the DABCO²⁺ would be beneficial to the formation of different hydrogen bonds between organic diamine cations and inorganic framework, which then influences the charge transfer by $N_{NH4}-H \cdots X$ interaction. However, the poor strength of interaction force makes the most advanced metal-free perovskite-based X-ray detector show retarded sensitivity of $1997 \pm 80 \mu C Gy_{air}^{-1} cm^{-2}$ at a small bias (50 V), which is far from the MHP-based one.^[13]

In addition to the number and strength of hydrogen-bonding interaction of metal-free perovskite, two main problems remain to be deeply explored in X-ray detection: One is the stability evaluation of metal-free perovskites under X-ray irradiation, since heat is usually associated with high-energy radiation.^[19,22] Meanwhile, theoretical considerations make it more challenging to evaluate the stability of metal-free perovskites through the traditional tolerance factor due to the large variation in bond lengths as a result of hydrogen bonding interactions.^[9,18] Another problem is that the practical applications for the fundamental advantages of metal-free perovskite should be further evaluated, which remains barely explored, especially in the integration of circuit, flexible and large-area devices. This is simply ascribed to that the recently

reported different kinds of metal-free perovskites were single crystal (SCs) with fragile, rigid and small-area properties.^[12,23]

In this work, we demonstrate the understanding of multiple hydrogen bonds metal-free PAZE-NH₄X₃·H₂O perovskite on X-ray application. Based on theoretical calculation, we elaborated their difference in the crystal structure and band nature with different halide components introduced. Subsequently, the advantages of metal-free perovskite are fully exploited to expand its practical X-ray application on the flexible substrate with excellent performance and stability, and the potential as a pixelated matrix to provide high spatial-resolution X-ray imaging.

Result and discussion

In this work, we have successfully synthesized the metal-free perovskite of PAZE-NH₄X₃·H₂O with different halide ions through a non-toxic solution method, as shown in Figure S1 (detailed synthesis procedure listed in “Supporting Information”). To further characterize the properties of PAZE-NH₄X₃·H₂O powders, multi-characterization methods are used to confirm its final products. First, nuclear magnetic resonance (NMR) and Fourier transform infrared (FT-IR) spectra are shown in Figure S2, where the integrated ratio of signals are corresponding well with the piperazine, indicating the high purity of raw materials.^[24] Besides, the bending vibration of δ(H₂O) appearing at ~1650 cm⁻¹ in FT-IR spectra further indicates the probable formation of PAZE-NH₄X₃·H₂O.^[25,26]

Furthermore, in thermogravimetric analysis (TGA), the most weight loss (~60%) point of PAZE-NH₄X₃·H₂O is around 350°C, as shown in Figure S3. The high temperature of weight loss suggests that the PAZE-NH₄X₃·H₂O constructed with hydrogen bonds would be comparable to the traditional MHPs of MAPbI₃ (348°C) and FAPbI₃ (363°C) consisting of coordination bonds.^[16,17,27] Then, scanning electron microscope (SEM) and energy-dispersive spectrometric (EDS) are further utilized to study their morphology properties and components difference in Figure S4. Both Br- and Cl-based PAZE-NH₄X₃·H₂O powders are stacked with many small particles to form rods with good crystallinity, while PAZE-NH₄I₃·H₂O shows extensive aggregation with square shape. Meanwhile, all the EDS mapping of PAZE-NH₄X₃·H₂O powders show well-distributed of C, N, O and halide elements. Also, the optical properties of

thick PAZE-NH₄X₃·H₂O films were performed on the quartz substrate (Figure S5), and showed a sharp drop at ≈ 186 , ≈ 204 and ≈ 210 nm for the Cl, Br and I-based PAZE-NH₄X₃·H₂O film.^[12]

The density functional theory (DFT) simulation is applied to explore the inherent properties of PAZE-NH₄X₃·H₂O with different halide components. Figure 1a displays the packing structure diagrams of these crystals in a specific direction, and all of them show similar structures. Besides, the structures of PAZE-NH₄X₃·H₂O perovskite crystals with a three-dimensional model of the stacking structure are shown in Figure S6. Each NH₄⁺ forms a distorted [NH₄]X₆ octahedron with the six adjacent halogen anions through hydrogen bonds, which are further jointed together in a vertex-sharing way to extend in three orthogonal directions. Thereinto, the protonated PAZE²⁺ cation is occupied in the central region of cage formed by eight octahedrons, in which H₂O molecules are situated on (001) plane.^[16,17] The difference in electronegativity of halogens from Cl to I results in different hydrogen bond (N-H...X) strength of PAZE-NH₄X₃·H₂O. Moreover, the strength of the hydrogen bond largely influences the crystal structure of metal-free perovskite. Therefore, the stronger strength and increasing number of hydrogen bonds would further improve the lattice stiffness for better endurance of X-ray radiation.^[17]

Subsequently, we fabricated PAZE-NH₄Br₃·H₂O SCs in Figure S7, and used it as an example in single-crystal X-ray diffraction to further confirm the rationality of the crystal structure (Table S1). The XRD pattern of PAZE-NH₄Br₃·H₂O SCs agrees well with its powder and simulation results in Figure 1b. The crystal exhibits two dominating

peaks at $2\theta = 13.7^\circ$ and 27.2° , which accord with the (002) and (004) planes, and belongs to the *Pbcm* space group of orthorhombic system with lattice parameters of $a = 6.7443(5) \text{ \AA}$, $b = 13.3989(8) \text{ \AA}$, $c = 13.1951(8) \text{ \AA}$. Besides, the corresponding XRD patterns of I- and Cl-based PAZE-NH₄X₃·H₂O correspond with their simulation values rigorously as well, as shown in Figure S8.

Moreover, the halide ions diffusion energy and band structure are well explored through DFT calculation for their significant influence on the X-ray device performance.^[11,28] In Figure 1c, the diffusion barriers of different halogens are calculated as 1.39, 1.41 and 1.79 eV for V_{Cl}, V_{Br} and V_I, respectively. This difference may be attributed to the different radii of halide components for the large radii less likely to induce migration.^[29] Furthermore, the larger diffusion barrier is beneficial to suppress the migration of halide ions, retard baseline drift and improve the stability of materials under high-energy ionization radiation.^[30] Notably, all the PAZE-NH₄X₃·H₂O display similar band structures with direct bandgap at Γ point due to the similar crystal structure for Cl (5.34 eV), Br (4.66 eV) and I (4.17 eV)-based crystal, as shown in Figures 1d-f. Apparently, the bandgaps gradually decrease with the increase of halogen radius from Cl to I, which is ascribed to the decreased electronegativity resulting in the increase of band dispersion and smaller bandgaps.^[17] The large bandgaps ($> 4.0 \text{ eV}$) of PAZE-NH₄X₃·H₂O make them show slight influence by ambient light, and ensure the device as excellent materials for X-ray detection (Figure S9). Besides, the partial density of states (pDOS) and charge-density distribution of PAZE-NH₄X₃·H₂O in Figures 1d-f and Figure S10 are also conducted to explore the band nature. For the

valence band maximum (VBM), it is contributed by the np orbitals of halides with few contributions of the O-2p and N-2p, while the conduction band minimum (CBM) is dominated by the C-2p, N-s and X-s. To further confirm the real contribution of N in VBM and CBM, we calculated the function of PAZE²⁺ and NH₄⁺ contribution in Figure S11, respectively. This result shows that the contribution from N in the VBM originates from NH₄⁺ while the N contribution in the CBM comes from PAZE²⁺. Therefore, for the dominating place of bivalent cation in the CBM, the bandgaps of metal-free perovskite could be modified by selecting rational organic A-site cations, which is corresponding to the previous report by Song et al. and Bie et al.^[15,31]

Moreover, metal-free PAZE-NH₄X₃·H₂O perovskite could be degraded under non-toxic solvent (Figure S12). Therefore, we take the advantages of metal-free perovskite in the flexible, bio-compatible and eco-friendly device preparation, and use the low-temperature spin-coating method to combine PAZE-NH₄X₃·H₂O on the flexible and transparent PEN substrate with thickness of 384.5 nm, as shown in Figure 2a. The SEM of PAZE-NH₄Br₃·H₂O on the PEN substrate shows a dense and flat morphology in Figure S13. Then, the transparency of PAZE-NH₄X₃·H₂O/PEN was tested through UV-vis spectra, and found that the deposited materials did not have much impact of the substrate transmittance in the range of visible light (Figure 2b).

Then, the ability of X-ray attenuation efficiency of PAZE-NH₄X₃·H₂O was further performed in a broad range of photon energies under X-ray illumination. The comparison of X-ray absorption capability of different X-ray materials including traditional semiconductors of Si, Ga₂O₃ and MHP (CsPbBr₃) is shown in Figure 2c.

According to the X-ray absorption formula of $\alpha \propto Z^4/E^3$ (Z is the atomic number of materials, E is the X-ray photon energy), the mass absorption efficiency is directly proportional to the Z value, which results in higher X-ray absorption in the Br- and I-based semiconductor than others.^[32,33] Therefore, the Br- and I-based PAZE-NH₄Br₃·H₂O perovskite exhibit a superior X-ray attenuation efficiency than the traditional Si, and is comparable to the MHP of CsPbBr₃ (Figure 2d). For 50 keV hard X-ray photons, a thickness of 1 mm is almost enough for PAZE-NH₄I₃·H₂O to completely attenuate X-ray photons, while it only achieves 20% attenuation for Si.^[28] The high X-ray attenuation efficiency is beneficial to generate enough carriers in absorbing material with limited thickness, which promotes the fabrication of low-cost and lightweight devices.^[34-36]

For X-ray detection applications, trap density, noise density and $\mu\tau$ are significant figures of merit, which are also evaluated to find the difference in PAZE-NH₄X₃·H₂O. The space charge limited current (SCLC) is applied with a simple device structure of Ag/PAZE-NH₄X₃·H₂O/Ag to deduce the trap density difference (Figure S14).^[37] The trap density (N_t) is calculated as $1.91 \times 10^{14} \text{ cm}^{-3}$, $1.71 \times 10^{14} \text{ cm}^{-3}$ and $2.21 \times 10^{15} \text{ cm}^{-3}$ for PAZE-NH₄X₃·H₂O with halide from Cl to I, which is comparable to the state of the art materials of Si (10^{13} - 10^{14} cm^{-3}) and CdTe (10^{11} - 10^{13} cm^{-3}).^[38,39] The difference in N_t density is probably caused by the different quality of crystallinity and improved strength of hydrogen bonds for stable crystal structure.^[12] Also, the noise density spectra of three different kinds of devices were performed in Figure S15. Obviously, the devices of Br- and I-based PAZE-NH₄X₃·H₂O possess lower noise than the Cl-based

one, which would be originated from the different ion diffusion energy with different halide as discussed above.^[40]

The parameter of $\mu\tau$ product for evaluating the charge extraction capability is obtained by fitting the X-ray photoconductivity curves by the Hecht equation, as shown in Figure 2e.^[41] The $\mu\tau$ product was achieved with value of 1.19×10^{-6} , 1.08×10^{-6} and $1.30\times 10^{-6} \text{ cm}^2 \text{ V}^{-1}$ for the Cl-, Br- and I-based films, respectively. Notably, these values not only are higher than some traditional materials films (Si, $10^{-7} \text{ cm}^2 \text{ V}^{-1}$), but also comparable to the partial MHP-based film ($\text{Cs}_{0.1}(\text{FA}_{0.83}\text{MA}_{0.17})_{0.9}\text{Pb}(\text{Br}_{0.17}\text{I}_{0.83})_3$, $2\times 10^{-6} \text{ cm}^2 \text{ V}^{-1}$).^[42,43] Therefore, based on the comprehensive consideration of X-ray attenuation capacity, hydrogen-bonding strength and crystal quality, PAZE- $\text{NH}_4\text{Br}_3\cdot\text{H}_2\text{O}$ would be selected as the main research object below.

Then, a flexible detector with PAZE- $\text{NH}_4\text{Br}_3\cdot\text{H}_2\text{O}$ is fabricated to evaluate its X-ray detection performance. The current-voltage (I-V) curves were obtained by switching X-ray on and off at dose rates in the range of 0.217 to $1.96 \text{ mGy}_{\text{air}} \text{ s}^{-1}$ with a bias from -20 to 20 V (Figure 3a). Notably, the photocurrent increases with the gradual increase of X-ray dose rate, and the dark current is always kept at low values (Figure 3b). Besides, the response time, defined as the response to rising (decay) from 10% (90%) to 90% (10%), is also used to measure the response-ability of the detector in Figure 3c and Figure S16. All the PAZE- $\text{NH}_4\text{X}_3\cdot\text{H}_2\text{O}$ exhibit fast-rising and decaying time of 10-25 ms, indicating their potential for dynamic imaging.^[44] Meanwhile, the stability of photocurrent is also conducted with a repeated voltage (+200 to 0 V) of 1650 s ($\Delta t = 30\text{s}$). The flexible detector shows remarkable stability in terms of its

photocurrent and dark current, indicating superior switching characteristics (Figure 3d). This conclusion is also confirmed by the I-V curves of repeating dose rate from 0.682 to 1.39 and final to 0.682 mGy_{air} s⁻¹ in Figure 3e.

Moreover, in Figure 3f, the relationship between the current density and dose rate of the PAZE-NH₄Br₃·H₂O flexible X-ray detector was performed under bias of 25, 50, 100, 150 and 200 V, and exhibits an approximately linear relationship between them. According to the slope of curves, the flexible devices deliver prominent sensitivity of 3708, 2833 and 2130 μC Gy_{air}⁻¹ cm⁻² for Br-, Cl- and I-based PAZE-NH₄X₃·H₂O under 20 keV X-ray photons at 200 V (Figure 3g), which is the highest value among all the metal-free perovskite X-ray detectors for PAZE-NH₄Br₃·H₂O device (Table S2). Besides, the device displays low dark current (Figure S17) with a low limit of detection (LoD) value of 0.192 μGy_{air}⁻¹ s⁻¹ (Figure 3h). Notably, the LoD value is lower than the required for regular medical diagnostics (5.5 μGy_{air} s⁻¹), and benefits to reduce the damage of organisms under the exposure to radiation.^[45] This different performance may be attributed to the combined effect of hydrogen bond strength and crystal quality, which results in different carrier mobilities, response times, X-ray attenuation and charge collection efficiency as previously mentioned. The comparison of sensitivity in flexible X-ray detectors with different kinds of semiconductors, including metal-free, organic and metal-containing (with or without Pb), are summarized in Figure 3i and Table S3. Notably, the sensitivity in this work exceeds most works of two-dimensional based MHP detector (PEA₂PbBr₃, 806 μC Gy_{air}⁻¹ cm⁻²) and all-inorganic MHP (CsPbBr₃, 1450 μC Gy_{air}⁻¹ cm⁻²), which is comparable to the most advanced Pb-based

MHP detectors ($\text{MAPb}(\text{I}_{0.9}\text{Cl}_{0.1})_3$, $8696 \pm 228 \mu\text{C Gy}_{\text{air}}^{-1} \text{ cm}^{-2}$) under low electric field.^[46-52]

Subsequently, the mechanical flexibility and stability of the device were further explored with different bending cycles (0-2500 cycles) and bending radii (∞ , 9.93, 8.94, 7.83 and 5.92 mm). The R_C defines as the different radii of bending curvatures, and one cycle defines as that the film is bent from the flat state to a certain bending radius and recovers to the initial state, as shown in Figure 4a. The currents were recorded by on/off X-ray source under a dose rate of $1.96 \text{ mGy}_{\text{air}} \text{ s}^{-1}$, and shows no obvious change in term of current with the increase of bending cycles (Figure 4b). Besides, the sensitivity of the detector maintains ~90% of its initial value after 2500 times bending cycles (Figure 4c). Meanwhile, the stability of current density under different bending radii is also conducted in Figures 4d, e. The device still maintains superior stability with the radius varying from ∞ to 5.92 mm under a high dose rate of $25.5 \text{ mGy}_{\text{air}} \text{ s}^{-1}$. Moreover, the stability of the device under extreme conditions was further tested. The International Standards (IEC 61646 climatic chamber tests) were used with a temperature range of -40 to 85°C for 5 times, as shown in Figure 4f.^[53] The $\text{PAZE-NH}_4\text{Br}_3 \cdot \text{H}_2\text{O}$ device exhibits better heating stability with small baseline drift than the I- and Cl-based for their difference in hydrogen bonds, ion diffusion energy and crystallinity (Figures S18a, b).^[5,11] Besides, the device stability under higher radiation energy of hard X-ray (160 keV) is also conducted, which exhibits better photocurrent stability, indicating a promising direction in industrial application, as shown in Figures S18 c, d.

Finally, the superior stability and better X-ray detection performance of the

flexible device impel us to evaluate the feasibility in a flexible and pixelated X-ray imager. Therefore, a 3×3 pixelated X-ray imager was manufactured to provide a proof-of-concept flexible imaging system using metal-free perovskite. The whole X-ray imaging process is shown in Figure 5a. The detector array could excite corresponding photocurrents when X-ray penetrates the flexible object at different positions. Then, the different intensity of current signals at each pixel was collected, and outlined the specific characteristics of the object.^[54,55] The 3×3 pixelated X-ray imager exhibits uniform photocurrent and dark current (Figure 5b), which ensures the quality of imaging figures.^[56,57] Subsequently, the advancement of the flexible detector was shown by placing curving “L”, “Z” and “U”-shaped copper plates on the bent and flat imager. According to the gradient photocurrent difference of each pixel, the rigid devices present more or less distortion for the non-uniform spatial distribution of X-ray dose, which is highlighted in Figure 5c.^[58] Differently, the flexible device could be comfortably attached to the curving object, and realize better imaging figures. Notably, the contrast between flexible and rigid images is not clear enough, which may be ascribed to the appearance of the signal/electrical crosstalk in the 3×3 pixelated X-ray imager. The contrast can be further optimized by reducing pixel size ($< 10 \mu\text{m}$) and a deep learning algorithm.^[41,59] Therefore, these different results adequately indicate the advantage of flexible devices in non-flat objects and narrow space imaging.^[7]

Meanwhile, the single-pixel imaging ability is also conducted by fitting the target object on a moving X-Y stage, and recording the different photocurrents of the detector. As shown in Figure 5d, the spatial resolution of the detector was researched with the

slanted-edge method at the modulation transfer function (MTF), which originates from the edge spread function (ESF) (Figure S19). Its value is largely determined by the pixel size, imaging distance and collimation degree.^[8] Therefore, the X-ray system based on high collimation and small-area ($0.2 \text{ mm} \times 0.5 \text{ mm}$) pixel delivers high spatial resolution of 5.00 lp mm^{-1} , which is the highest value in the flexible X-ray detectors.^[11,60] Finally, in Figure 5e, an imaging object was hidden in a plastic box, and the basic outlines of a deer with its ears can be observed, indicating its promising application in safety inspection field. This simple imaging ability further broaden the potential application in X-ray imaging of metal-free perovskite.

Conclusion

In conclusion, a kind of promising lightweight, bio-compatible and eco-friendly metal-free PAZE-NH₄X₃·H₂O perovskite with strengthened hydrogen bonds is successfully fabricated and delicately introduced into the X-ray detection for their unique crystal structure, high ions diffusion energy and decent photoelectric properties. Based on the theoretical simulation, the stronger strength and increasing number of hydrogen bonds in PAZE-NH₄X₃·H₂O tend to improve the lattice stiffness for better endurance of X-ray radiation. Besides, the large bandgaps make them show slight influence by ambient light, and could be modified by selecting rational organic A-site cations for the special contribution of PAZE²⁺ in the CBM. Moreover, combining the advantages of low trap density ($1.71 \times 10^{14} \text{ cm}^{-3}$), high $\mu\tau$ products ($1.06 \times 10^{-6} \text{ cm}^2 \text{ V}^{-1}$) and quick response time (10-20 ms), the PAZE-NH₄Br₃·H₂O is expanded into the flexible and transparent X-ray detector with the highest sensitivity of up to 3708 $\mu\text{C Gy}_{\text{air}}^{-1} \text{ cm}^{-2}$ among metal-free perovskites, which is comparable to the most advanced MHP-based flexible X-ray detector. Meanwhile, the flexible X-ray detector exhibits remarkable stability in periodic bending (0 to 2500 times), large bending radius (∞ to 5.92 mm) and long-term temperature aging (-40 to 85°C). Finally, the flexible PAZE-NH₄X₃·H₂O detector obtains the highest spatial resolution of 5.0 lp mm⁻¹ with clear imaging figures. In short, this work systematically exploited the advantages of metal-free perovskite in practical X-ray application, and emphasizes their potential as pixelated matrix to provide high spatial-resolution imaging.

Acknowledgments

This work was funded by the National Natural Science Foundation of China (52073131, 12047501 and 12047501), the Fundamental Research Funds for the Central Universities (lzujbky-2021-it31), and the calculation work was supported by Supercomputing Center of Lanzhou University.

Competing Financial Interests

The authors declare no competing financial interests.

Author Contributions Statement

Z.L., C.S., and Z.J. performed the experiments, data analysis, and experimental planning. Z.H.L. performed the DFT calculation section. The project was conceived, planned, and supervised by Z.J. Some of the experimental tests were supported by G.P. and H.C. The manuscript was written by Z.L. and Z.J. All the authors reviewed the manuscript.

Reference

- [1] Y. He, I. Hadar, M. G. Kanatzidis, *Nat. Photon.* **2021**, *16*, 14-26.
- [2] R. Zhuang, X. Wang, W. Ma, Y. Wu, X. Chen, L. Tang, H. Zhu, J. Liu, L. Wu, W. Zhou, X. Liu, Y. Yang, *Nat. Photon.* **2019**, *13*, 602-608.
- [3] X. Ou, X. Qin, B. Huang, J. Zan, Q. Wu, Z. Hong, L. Xie, H. Bian, Z. Yi, X. Chen, Y. Wu, X. Song, J. Li, Q. Chen, H. Yang, X. Liu, *Nature* **2021**, *590*, 410-415.
- [4] Y. C. Kim, K. H. Kim, D.-Y. Son, D.-N. Jeong, J.-Y. Seo, Y. S. Choi, I. T. Han, S. Y. Lee, N.-G. Park, *Nature* **2017**, *550*, 87-91.
- [5] Y. Zhou, L. Zhao, Z. Ni, S. Xu, J. Zhao, X. Xiao, J. Huang, *Sci. Adv.* **2021**, *7*, eabg6716.
- [6] H. Wei, J. Huang, *Nat. Commun.* **2019**, *10*, 1066.
- [7] J. Zhao, L. Zhao, Y. Deng, X. Xiao, Z. Ni, S. Xu, J. Huang, *Nat. Photon.* **2020**, *14*, 612-617.
- [8] W. Wei, Y. Zhang, Q. Xu, H. Wei, Y. Fang, Q. Wang, Y. Deng, T. Li, A. Gruverman, L. Cao, J. Huang, *Nat. Photon.* **2017**, *11*, 315-321.
- [9] X. Song, G. Hodes, K. Zhao, S. Liu, *Adv. Energy Mater.* **2021**, *11*, 2003331.
- [10] L. Li, Y. Yu, P. Li, J. Liu, L. Liang, L. Wang, Y. Ding, X. Han, J. Ji, S. Chen, D. Li, P. Liu, S. Zhang, M. Zeng, L. Fu, *Adv. Mater.* **2022**, *34*, 2108396.
- [11] B. Yang, W. Pan, H. Wu, G. Niu, J.-H. Yuan, K.-H. Xue, L. Yin, X. Du, X.-S. Miao, X. Yang, Q. Xie, J. Tang, *Nat. Commun.* **2019**, *10*, 1989.
- [12] Q. Cui, X. Song, Y. Liu, Z. Xu, H. Ye, Z. Yang, K. Zhao, S. Liu, *Matter* **2021**, *4*, 2490-2507.
- [13] X. Song, Q. Li, J. Han, C. Ma, Z. Xu, H. Li, P. Wang, Z. Yang, Q. Cui, L. Gao, Z. Quan, S. F. Liu, K. Zhao, *Adv. Mater.* **2021**, *33*, 2102190.
- [14] H. Morita, R. Tsunashima, S. Nishihara, K. Inoue, Y. Omura, Y. Suzuki, J. Kawamata, N. Hoshino, T. Akutagawa, *Angew. Chem. Int. Ed.* **2019**, *58*, 9184-9187.
- [15] X. Song, Q. Cui, Y. Liu, Z. Xu, H. Cohen, C. Ma, Y. Fan, Y. Zhang, H. Ye, Z. Peng, R. Li, Y. Chen, J. Wang, H. Sun, Z. Yang, Z. Liu, Z. Yang, W. Huang, G. Hodes, S. F. Liu, K. Zhao, *Adv. Mater.* **2020**, *32*, 2003353.
- [16] Colin A. Bremner, Michael Simpson, William T. A. Harrison, *J. Am. Chem. Soc.* **2002**, *124*, 10960-10961.
- [17] K. Li, L.-Y. Dong, H.-X. Xu, Y. Qin, Z.-G. Li, M. Azeem, W. Li, X.-H. Bu, *Mater. Chem. Front.* **2019**, *3*, 1678-1685.
- [18] H.-Y. Ye, Y.-Y. Tang, P.-F. Li, W.-Q. Liao, J.-X. Gao, X.-N. Hua, H. Cai, P.-P. Shi, Y.-M. You, R.-G. Xiong, *Science* **2018**, *361*, 151-155.
- [19] H. S. Choi, S. Li, I.-H. Park, W. H. Liew, Z. Zhu, K. C. Kwon, L. Wang, I.-H. Oh, S. Zheng, C. Su, Q.-H. Xu, K. Yao, F. Pan, K. P. Loh, *Nat. Commun.* **2022**, *13*, 794.
- [20] R. Gao, X. Shi, J. Wang, G. Zhang, H. Huang, *Adv. Funct. Mater.* **2021**, *31*, 2104393.
- [21] H.-S. Wu, B. T. Murti, J. Singh, P.-K. Yang, M.-L. Tsai, *Adv. Sci.* **2022**, *9*, 2104703.
- [22] D. Yu, P. Wang, F. Cao, Y. Gu, J. Liu, Z. Han, B. Huang, Y. Zou, X. Xu, H. Zeng, *Nat. Commun.* **2020**, *11*, 3395.
- [23] L.-L. Chu, T. Zhang, W.-Y. Zhang, P.-P. Shi, J.-X. Gao, Q. Ye, D.-W. Fu, *J. Phys. Chem. Lett.* **2020**, *11*, 1668-1674.
- [24] Z. Li, B. Ma, Y. Xu, Y. Lei, W. Lan, G. Wang, W. Li, Q. Wang, H. L. Zhang, Z. Jin, *Adv. Funct. Mater.* **2021**, *31*, 2106380.
- [25] L. Ding, M. Li, Y. Zhao, H. Zhang, J. Shang, J. Zhong, H. Sheng, C. Chen, J. Zhao, *Appl. Catal. B* **2020**, *266*, 118634.

- [26] R. M. A. Vergauwe, A. Thomas, K. Nagarajan, A. Shalabney, J. George, T. Chervy, M. Seidel, E. Devaux, V. Torbeev, T. W. Ebbesen, *Angew. Chem. Int. Ed.* **2019**, *58*, 15324-15328.
- [27] L. Ma, D. Guo, M. Li, C. Wang, Z. Zhou, X. Zhao, F. Zhang, Z. Ao, Z. Nie, *Chem. Mater.* **2019**, *31*, 8515-8522.
- [28] W. Pan, H. Wu, J. Luo, Z. Deng, C. Ge, C. Chen, X. Jiang, W.-J. Yin, G. Niu, L. Zhu, L. Yin, Y. Zhou, Q. Xie, X. Ke, M. Sui, J. Tang, *Nat. Photon.* **2017**, *11*, 726-732.
- [29] X. Wang, Y. Ling, X. Lian, Y. Xin, K. B. Dhungana, F. Perez-Orive, J. Knox, Z. Chen, Y. Zhou, D. Beery, K. Hanson, J. Shi, S. Lin, H. Gao, *Nat. Commun.* **2019**, *10*, 695.
- [30] X. Zhang, T. Zhu, C. Ji, Y. Yao, J. Luo, *J. Am. Chem. Soc.* **2021**, *143*, 20802-20810.
- [31] J. Bie, D.-B. Yang, M.-G. Ju, Q. Pan, Y.-M. You, W. Fa, X. C. Zeng, S. Chen, *JACS Au* **2021**, *1*, 475-483.
- [32] H. Chen, Q. Wang, G. Peng, S. Wang, Y. Lei, H. Wang, Z. Yang, J. Sun, N. Li, L. Zhao, W. Lan, Z. Jin, *Adv. Opt. Mater.* **2022**, *10*, 2102790.
- [33] S. Tie, W. Zhao, D. Xin, M. Zhang, J. Long, Q. Chen, X. Zheng, J. Zhu, W.-H. Zhang, *Adv. Mater.* **2020**, *32*, 2001981.
- [34] Y. Zhou, J. Chen, O. M. Bakr, O. F. Mohammed, *ACS Energy Lett.* **2021**, *6*, 739-768.
- [35] G. Kakavelakis, M. Gedda, A. Panagiotopoulos, E. Kymakis, T. D. Anthopoulos, K. Petridis, *Adv. Sci.* **2020**, *7*, 2002098.
- [36] F. Cao, D. Yu, W. Ma, X. Xu, B. Cai, Y. M. Yang, S. Liu, L. He, Y. Ke, S. Lan, K.-L. Choy, H. Zeng, *ACS Nano* **2019**, *14*, 5183-5193.
- [37] Y. Cheng, L. Ding, *SusMat* **2021**, *1*, 324-344.
- [38] J. R. Ayres, *J. Appl. Phys.* **1993**, *74*, 1787-1792.
- [39] A. Balcioglu, R. K. Ahrenkiel, F. Hasoon, *J. Appl. Phys.* **2000**, *88*, 7175-7178.
- [40] J. Peng, C. Q. Xia, Y. Xu, R. Li, L. Cui, J. K. Clegg, L. M. Herz, M. B. Johnston, Q. Lin, *Nat. Commun.* **2021**, *12*, 1531.
- [41] Z. Li, F. Zhou, H. Yao, Z. Ci, Z. Yang, Z. Jin, *Mater. Today* **2021**, *48*, 155-175.
- [42] S. O. Kasap, *J. Phys. D: Appl. Phys.* **2000**, *33*, 2853.
- [43] H. Mescher, F. Schackmar, H. Eggers, T. Abzieher, M. Zuber, E. Hamann, T. Baumbach, B. S. Richards, G. Hernandez-Sosa, U. W. Paetzold, U. Lemmer, *ACS Appl. Mater. Interfaces.* **2020**, *12*, 15774-15784.
- [44] Y. He, L. Matei, H. J. Jung, K. M. McCall, M. Chen, C. C. Stoumpos, Z. Liu, J. A. Peters, D. Y. Chung, B. W. Wessels, M. R. Wasielewski, V. P. Dravid, A. Burger, M. G. Kanatzidis, *Nat. Commun.* **2018**, *9*, 1609.
- [45] F. Zhou, Z. Li, W. Lan, Q. Wang, Z. Jin, *Small Methods* **2020**, *4*, 2000506.
- [46] J. Guo, Y. Xu, W. Yang, B. Xiao, Q. Sun, X. Zhang, B. Zhang, M. Zhu, W. Jie, *ACS Appl. Mater. Interfaces.* **2021**, *13*, 23928-23935.
- [47] H. Liang, S. Cui, R. Su, P. Guan, Y. He, L. Yang, L. Chen, Y. Zhang, Z. Mei, X. Du, *ACS Photon.* **2018**, *6*, 351-359.
- [48] C. Li, S. Zhou, J. Nie, J. Huang, X. Ouyang, Q. Xu, *Nano Lett.* **2021**, *21*, 10279-10283.
- [49] L. Basirico, A. Ciavatti, T. Cramer, P. Cosseddu, A. Bonfiglio, B. Fraboni, *Nat. Commun.* **2016**, *7*, 13063.
- [50] J. Liu, B. Shabbir, C. Wang, T. Wan, Q. Ou, P. Yu, A. Tadich, X. Jiao, D. Chu, D. Qi, D. Li, R. Kan, Y. Huang, Y. Dong, J. Jasieniak, Y. Zhang, Q. Bao, *Adv. Mater.* **2019**, *31*, 1901644.
- [51] A. Ciavatti, R. Sorrentino, L. Basirico, B. Passarella, M. Caironi, A. Petrozza, B. Fraboni, *Adv.*

- Funct. Mater.* **2021**, *31*, 2009072.
- [52] Z. Li, S. Chang, H. Zhang, Y. Hu, Y. Huang, L. Au, S. Ren, *Nano Lett.* **2021**, *21*, 6983-6989.
- [53] M. T. Hoang, Y. Yang, B. Tuten, H. Wang, *J. Phys. Chem. Lett.* **2022**, *13*, 2908-2920.
- [54] J. Chen, X. Liu, Z. Li, F. Cao, X. Lu, X. Fang, *Adv. Funct. Mater.* **2022**, *32*, 2201066.
- [55] H. Li, J. Song, W. Pan, D. Xu, W.-A. Zhu, H. Wei, B. Yang, *Adv. Mater.* **2020**, *32*, 2003790.
- [56] X. Li, P. Zhang, Y. Hua, F. Cui, X. Sun, L. Liu, Y. Bi, Z. Yue, G. Zhang, X. Tao, *ACS Appl. Mater. Interfaces.* **2022**, *14*, 9340-9351.
- [57] P. Zhang, Y. Hua, Y. Xu, Q. Sun, X. Li, F. Cui, L. Liu, Y. Bi, G. Zhang, X. Tao, *Adv. Mater.* **2022**, *34*, 2106562.
- [58] L. Han, B. Sun, C. Guo, G. Peng, H. Chen, Z. Yang, N. Li, Z. Ci, Z. Jin, *Adv. Opt. Mater.* **2022**, *10*, 2102453.
- [59] T. Kim, S. Jeong, K.-H. Kim, H. Shim, D. Kim, H.-J. Kim, *ACS Appl. Mater. Interfaces.* **2022**, *14*, 26004–26013.
- [60] Y. Song, L. Li, M. Hao, W. Bi, A. Wang, Y. Kang, H. Li, X. Li, Y. Fang, D. Yang, Q. Dong, *Adv. Mater.* **2021**, *33*, 2103078.

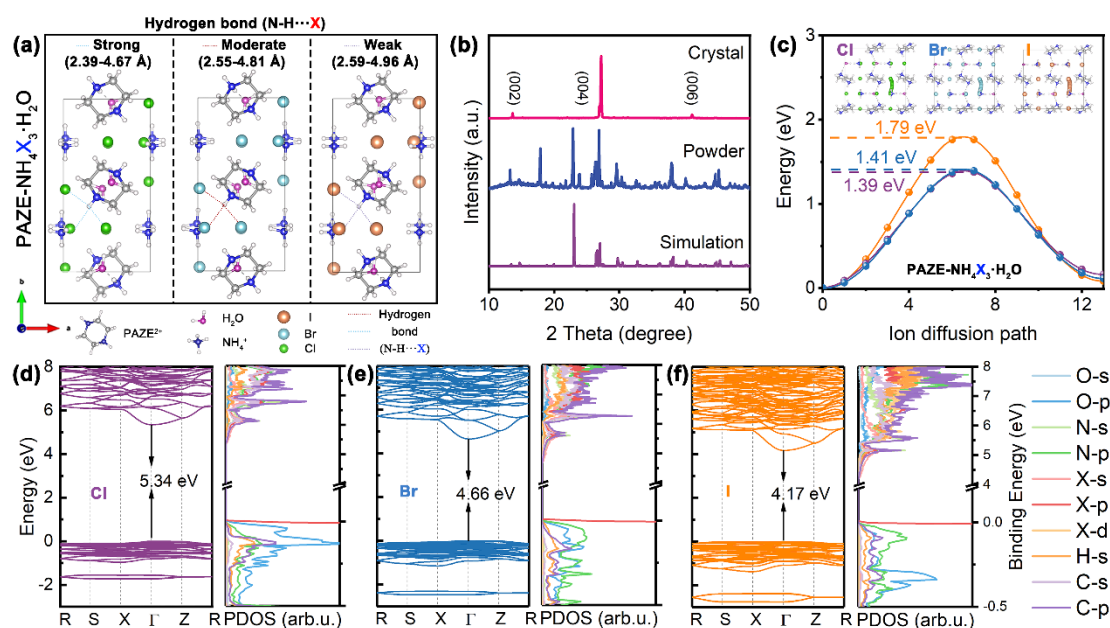


Figure 1. DFT calculation for the crystal structure, ion diffusion path and band nature of $\text{PAZE-NH}_4\text{X}_3 \cdot \text{H}_2\text{O}$: (a) Crystal structures and different strength of hydrogen bonds; (b) XRD patterns of the $\text{PAZE-NH}_4\text{Br}_3 \cdot \text{H}_2\text{O}$ with single crystal, powder and its simulation; (c) Calculated energy profile along the ionic migration path for the possible halides ion vacancies in $\text{PAZE-NH}_4\text{X}_3 \cdot \text{H}_2\text{O}$. Inset: Migration path of these ion vacancies; The energy band and calculated electronic density of states of the (d) Cl-, (e) Br- and (f) I-based $\text{PAZE-NH}_4\text{X}_3 \cdot \text{H}_2\text{O}$.

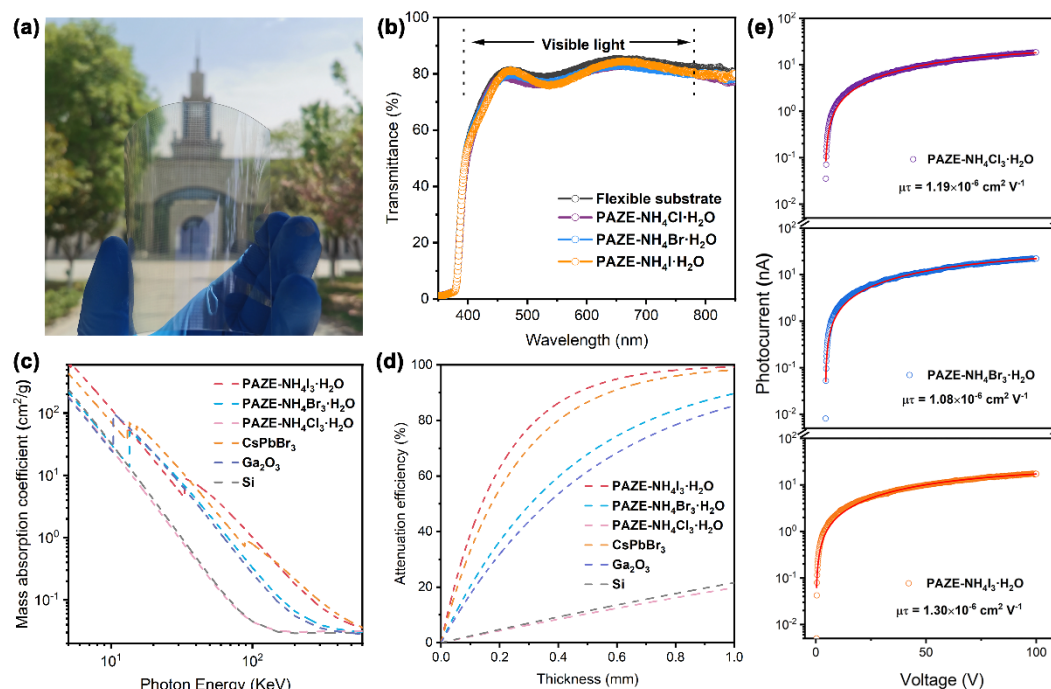


Figure 2. Optical and electronic properties of PAZE-NH₄X₃·H₂O: (a) Optical image of the fabricated flexible X-ray detectors; (b) Transmittance spectra; (c) Mass absorption coefficients as a function of photon energy and (d) Attenuation efficiency of 50 keV X-ray photons versus thickness for PAZE-NH₄X₃·H₂O, CsPbBr₃, Ga₂O₃ and Si; (e) Bias-dependent photoconductivity of PAZE-NH₄X₃·H₂O flexible X-ray detectors.

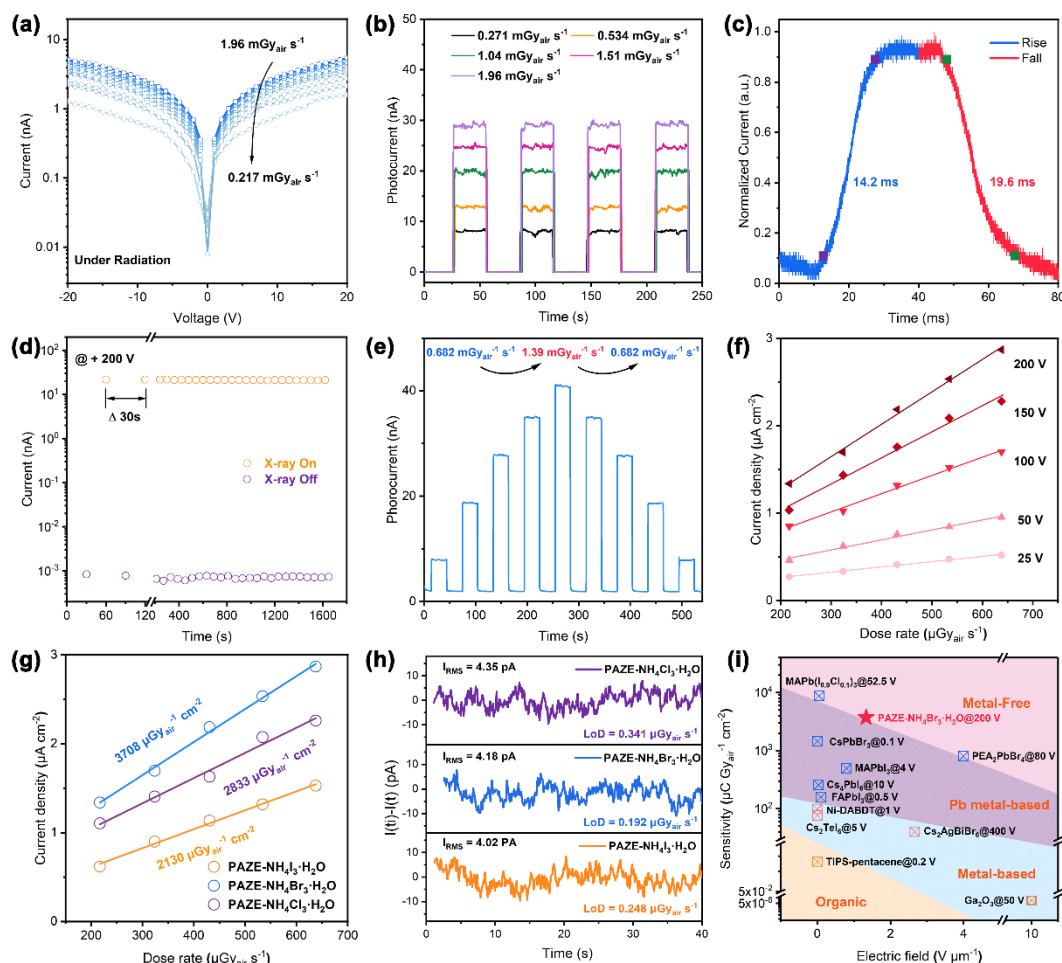


Figure 3. X-ray performance of PAZE-NH₄X₃·H₂O based flexible X-ray detectors: (a) The irradiated J-V curves measured at different dose rates; (b) Photocurrent signal dynamic versus time under different dose rates; (c) Time response; (d) The long-term stability of photocurrent and dark current under switching X-ray sources; (e) Photocurrent stability under different dose rates; (f) X-ray response of current density with various dose rates at different bias; (g) X-ray photocurrents as a function of dose rate; (h) Corresponding LoD values; and (i) The performance comparison of the reported flexible X-ray detectors under different biases and electric fields.

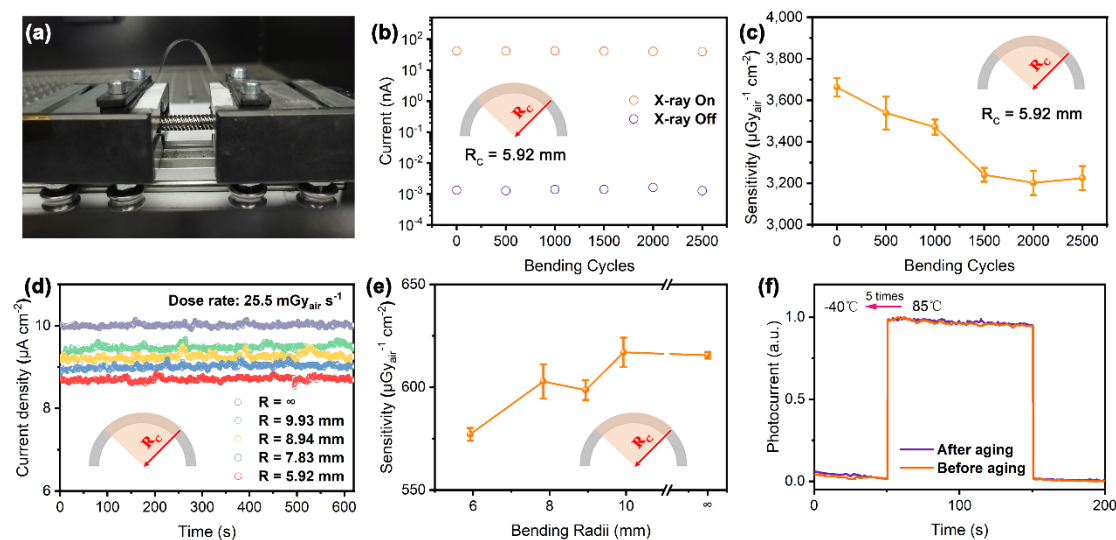


Figure 4. Bending and temperature-aging stability of PAZE-NH₄Br₃·H₂O flexible X-ray detectors: (a) Optical image of the bending system; (b) The stability of on-off current and (c) Sensitivity under the periodic bending of a bending radius of 5.92 mm at a dose rate of $1.96 \text{ mGy}_{\text{air}} \text{ s}^{-1}$; (d) The stability of on-off current and (e) Sensitivity under different bending radii at a dose rate of $25.5 \text{ mGy}_{\text{air}} \text{ s}^{-1}$; (f) Photocurrent stability of aging device over a wide temperature range.

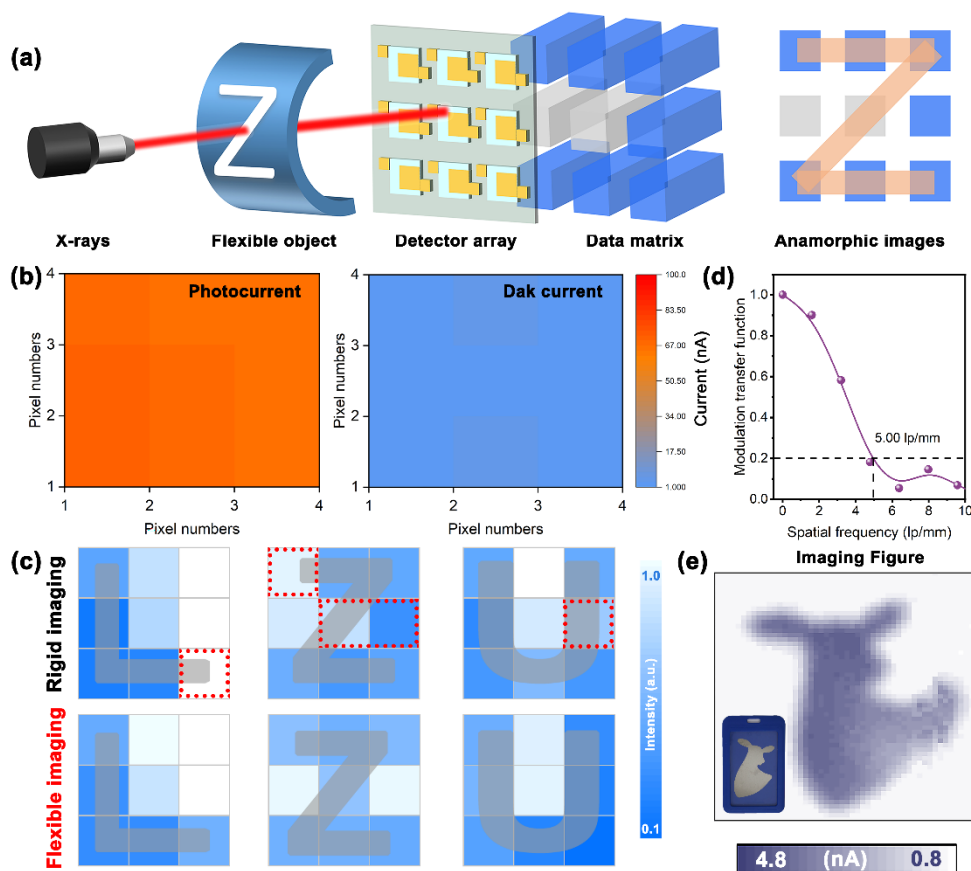


Figure 5. Imaging properties of the PAZE-NH₄Br₃·H₂O flexible X-ray detectors: (a) Schematic illustration of the X-ray imaging process; (b) Dark current and photocurrent mapping for the PAZE-NH₄Br₃·H₂O flexible X-ray detector array with 3 × 3 pixels; (c) Pixelated X-ray image of rigid and flexible imaging (red box is the anamorphic part); (d) The MTF as a function of the spatial frequency of the single-pixel detector, and (e) The corresponding X-ray image. Insert: optical graph of the imaging object in the blue plastic box.